Hindawi
International Journal of Energy Research
Volume 2023, Article ID 2200257, 15 pages
https://doi.org/10.1155/2023/2200257

Research Article

Lithiophilic and Conductive CuO-Cu_2O-Cu Microspheres with Controlled Void Structure via Spray Pyrolysis for Improved Lithium Metal Anode Performance

Jae Hun Choi,[1] **Jae Wook Kang**,[1] **Hye Young Koo**,[2] **and Yun Chan Kang**[1]

[1]*Department of Materials Science and Engineering, Korea University, Anam-dong, Seongbuk-gu, Seoul 136-713, Republic of Korea*
[2]*Department of Metal Powder, Korea Institute of Materials Science, 797 Changwon-daero, Changwon, Gyeongnam 51508, Republic of Korea*

Correspondence should be addressed to Hye Young Koo; hykoo@kims.re.kr and Yun Chan Kang; yckang@korea.ac.kr

Received 3 July 2023; Revised 11 September 2023; Accepted 21 September 2023; Published 20 October 2023

Academic Editor: Weiwei Han

Lithium metal anodes (LMAs) have attracted significant attention owing to their high theoretical capacity and lowest redox potential. However, dendritic growth of lithium limits its practical application. Controlling lithium deposition through structuring host materials for LMAs has been widely studied. In this study, a unique structured CuO-Cu_2O-Cu composite microsphere is synthesized through facile one-step spray pyrolysis process as a new lithium host material for LMAs. During lithium deposition, lithium ions preferred to be adsorbed on composite microspheres due to the electric field generated from the metallic Cu-based conductive matrix. The adsorbed ions reacted with lithiophilic copper oxides to form copper and Li_2O, promoting the generation of a uniform electric field and ion transfer. Moreover, hollow structure can guide lithium to be encapsulated inside the structures, enabling effective suppression of dendritic lithium growth. As a result, this composite microsphere is capable to store lithium with high areal capacity of 5.0 mAh cm^{-2} without dendritic growth of lithium. Consequently, the composite microspheres exhibit a coulombic efficiency above 99% for more than 200 cycles at a current density of 1.0 mA cm^{-2} as an asymmetric cell and show low voltage hysteresis of 19 mV for more than 1,000 h as a symmetric cell. This study demonstrates that the designed microstructures with an appropriate ratio of conductive and lithiophilic matrices with sufficient pore structures provide promising cycle performance as host materials for lithium metal anode.

1. Introduction

Lithium-ion batteries have received enormous attention as a representative electrochemical energy storage system. However, commercial anode graphite cannot satisfy the ever-growing demands for electric vehicles and grid energy storage systems owing to its low theoretical specific capacity of 372 mAh g^{-1} [1, 2]. Lithium metal is considered a highly desirable anode material for batteries because of its high theoretical specific capacity of 3,860 mAh g^{-1} and the lowest redox potential (-3.04 V vs. Li/Li^+) compared to other metals [3–5]. In addition, lithium metal anodes (LMAs) are paired with desirable lithium-sulfur and lithium-oxygen batteries, which are regarded as promising candidates for the next-generation battery systems [6, 7]. However, LMAs suffer from drawbacks preventing their commercialization as a battery system. One of the main issues is that lithium metal is highly reactive and can form dendrites, which are needle-like protrusions that can short-circuit the battery [8]. These dendrites can also grow into the electrolyte, which can lead to the formation of a solid electrolyte interface (SEI) on the surface of the lithium metal [9, 10]. This can reduce coulombic efficiency and capacity of the battery.

To overcome the issues associated with LMAs, researchers have developed several strategies, including the use of lithium alloys, artificial SEIs, protection layers, and separator modification [11–18]. Although these approaches could somewhat prevent lithium dendrite growth, considerable volume expansion still needs to be managed when operating under high areal capacity and current density.

The theoretical thickness of lithium deposition with an area capacity of 10.0 mAh cm^{-2} was calculated to be 48.5 μm cm^{-2}, and such large volume changes can cause deterioration of the mechanical properties of the SEI layer and poor coulombic efficiency and cycle stability of LMAs [19, 20]. Therefore, the host materials with an appropriately designed matrix for lithium plating and stripping are critical for suppressing volume fluctuation and dendritic lithium growth during cycles by regulating lithium plating and stripping behavior [9, 18, 21–23].

The dendritic growth of lithium is principally generated by the nonuniform distribution of current density on the surface of the current collector [24, 25]. Lithium ions can be uniformly distributed on the lithiophilic matrix and conductive matrix, resulting in suppressed dendritic lithium growth [10, 26–28]. In addition, the three-dimensional host materials with an improved surface area compared with the two-dimensional Cu foil current collector can lower the local current density [29, 30]. The lithiophilic matrix can lower the nucleation overpotential for lithium deposition on the surface of the electrode through chemical binding interactions between the lithiophilic matrix and lithium metal [31, 32]. Ruan et al. introduced TiO_2/Cu_2O heterostructure constructed on Cu foil, realizing stable lithium plating and stripping at the current density of 1 mA cm^{-2} [33]. Lithium ions tend to be adsorbed on TiO_2 by Ti-O binding, and lithium ions were reacted with Cu_2O from Cu and Li_2O, which resulted in lower nucleation overpotential and uniform lithium deposition on the surface. In contrast, the conductive matrix can form a uniform electric field on its surface; therefore, lithium ions deposit on the surface of the conductive matrix rather than the surface of previously deposited lithium [34–36]. Lu et al. used Cu nanowire as a freestanding current collector to store lithium metal inside the porous structure [37]. With the high surface area and high conductivity of nanowires, 7.5 mAh cm^{-2} of lithium could be plated. Based on the aforementioned considerations, integrating the merits of a lithiophilic matrix and a conductive matrix into one host structure could help to fabricate promising LMAs with high performances.

Herein, we prepared CuO-Cu_2O-Cu composite microspheres through a one-step spray pyrolysis system, denoted as CuO_x/Cu-PS1. The spray pyrolysis of an aqueous solution containing copper nitrate and proper amount of polystyrene (PS) nanobeads at 700°C under a nitrogen atmosphere resulted in hollow structured microspheres composed of CuO, Cu_2O, and Cu crystals. By adjusting the amount of PS nanobeads, the ratio between CuO, Cu_2O, and Cu crystals and the structures of microspheres could be changed. This work optimized lithium metal host structures by comparing the ratios of composite lithiophilic matrix and conductive matrix and achieved excellent cell performances through a facile one-step spray pyrolysis process. In addition, the hollow structure of composite materials could guide lithium to internal void space, resulted in the suppression of volume fluctuation and dendritic growth of lithium. Based on the above merits, CuO_x/Cu-PS1 microspheres as host materials for LMAs showed uniform lithium plating behavior without lithium dendrite formation. When operating with lithium foil as a counter electrode, CuO_x/Cu-PS1 microspheres exhibited stable cycle performance for more than 200 cycles with a coulombic efficiency of over 99% at a current density of 1.0 mA cm^{-2} with an areal capacity of 1.0 mAh cm^{-2}. Furthermore, lithium-plated CuO_x/Cu-PS1 microspheres displayed less than 20 mV of voltage hysteresis lasting for more than 2,500 h in symmetric cells. The strategies and synthetic process used in this work could be applied to the fabrication of other lithium metal host structures.

2. Experimental

CuO_x/Cu-PS1 microspheres were prepared through a spray pyrolysis process. The precursor solution contained 0.2 M copper nitrate and 30 mg mL^{-1} of 100 nm PS nanobeads in distilled water. Droplets generated by 1.7 MHz ultrasonic spray generator and N_2 gas with a flow rate of 10 L min^{-1} were used as carrier gas. The reactor temperature was maintained at 700°C. The precursor solution for CuO_x/Cu-PS3 and CuO_x/Cu-PS3 microspheres contained 90 and 150 mg mL^{-1} of 100 nm PS nanobeads, and CuO-PS0 microspheres were made without PS nanobeads. The rest of synthesis procedure was identical.

Experimental information on the material characterization and the electrochemical measurement is provided in the supporting information.

3. Results and Discussion

The formation mechanism of CuO_x/Cu-PS1 hollow microspheres is shown in Scheme 1. CuO_x/Cu-PS1 microspheres and their comparative samples were obtained via spray pyrolysis of an aqueous solution containing copper nitrate and PS nanobeads at 700°C under a nitrogen atmosphere. The comparative samples were prepared with three and five times as many PS nanobeads as CuO_x/Cu-PS1 microspheres, denoted as CuO_x/Cu-PS3 and CuO_x/Cu-PS5, respectively. During the spray pyrolysis process, droplets passed through a tube furnace, and rapid evaporation of droplets progressed from the surface of the droplets, forming hollow structured CuO microspheres with PS nanobeads [38]. Subsequently, PS nanobeads containing reducing elements (C and H) were decomposed to gaseous fragments, and the reduction of CuO to Cu_2O and Cu_2O to Cu proceeded [39]. Therefore, the amount of PS nanobeads affected the ratio of CuO, Cu_2O, and Cu. Following the decomposition of PS nanobeads, mesopores formed by PS nanobeads were filled by the sintering of metallic copper. Sintering of metallic copper progressed even inside the hollow space of microspheres and filled the void space of the structure as more metallic copper was reduced by more PS nanobeads in the case of CuO_x/Cu-PS3 and CuO_x/Cu-PS5 microspheres [39].

The morphology of CuO_x/Cu-PS1 microspheres obtained by one-step spray pyrolysis process is presented in Figure 1. SEM and TEM images of CuO_x/Cu-PS1 microspheres in Figures 1(a)–1(c) show that hollow and yolk-shell structured composite microspheres were composed of several tens of nanometer-sized crystals. The yolk part of CuO_x/Cu-PS1 microspheres might have been generated from the sintering

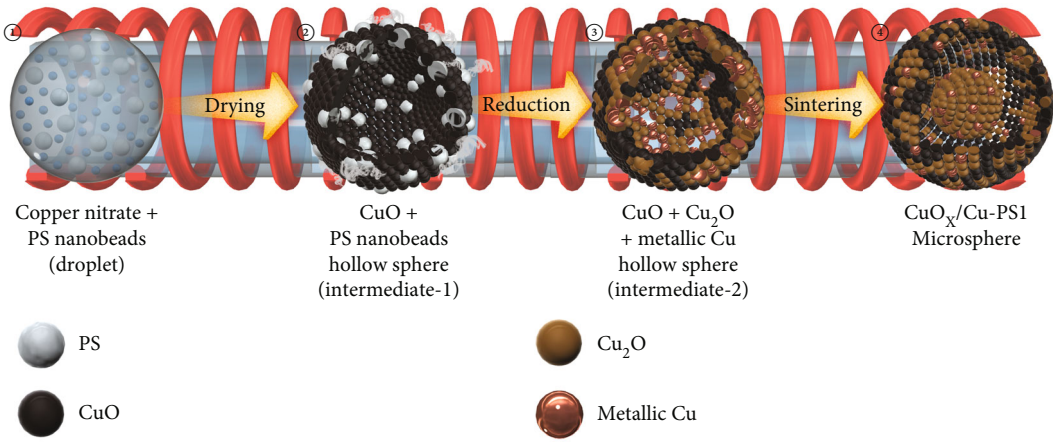

Scheme 1: Formation mechanism of CuO_x/Cu-PS1 microsphere.

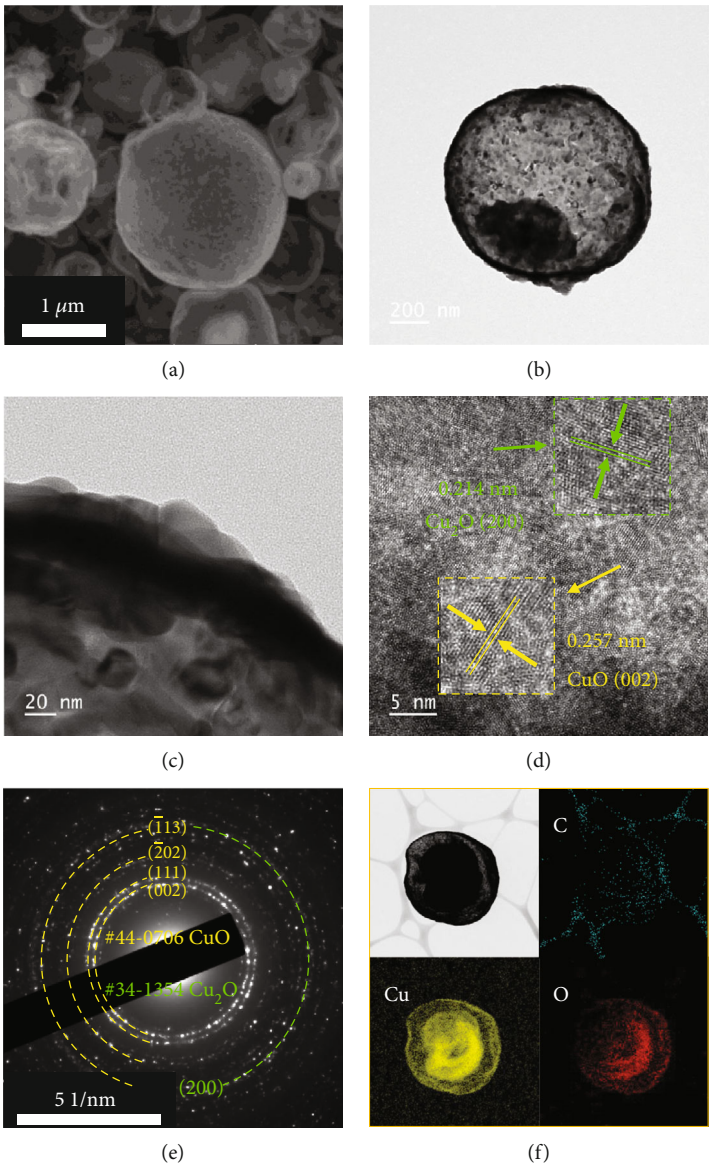

(a) (b) (c) (d) (e) (f)

Figure 1: Morphologies of CuO_x/Cu-PS1 microsphere obtained by spray pyrolysis: (a) SEM image, (b, c) TEM images, (d) HR-TEM image, (e) SAED pattern, and (f) elemental mapping images.

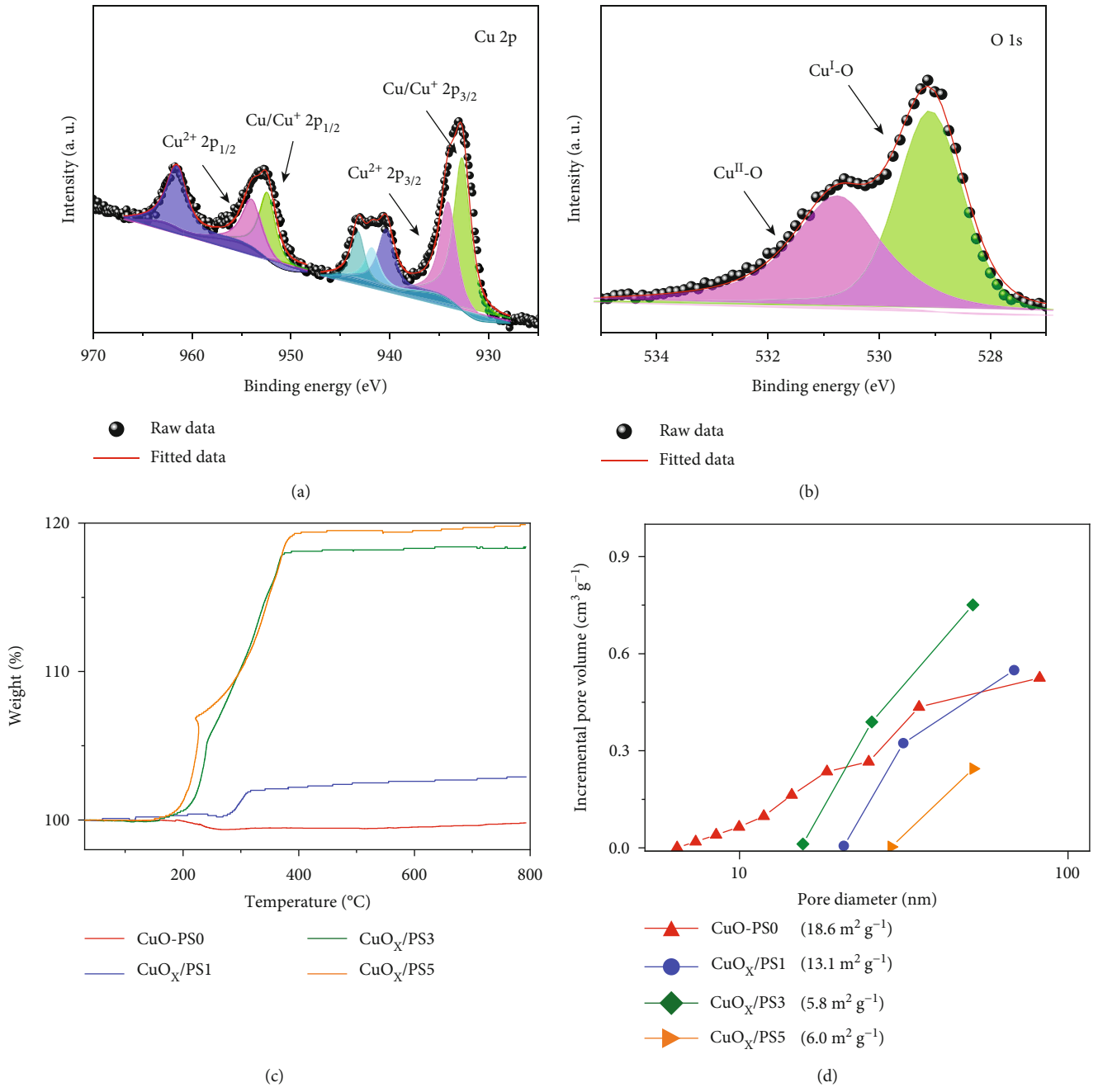

Figure 2: (a, b) XPS spectra of CuO_x/Cu-PS1 microsphere: (a) Cu 2p and (b) O 1s, (c) TGA curves, and (d) BJH pore size distribution corresponding to the CuO_x/Cu composite microspheres.

of metallic copper during synthesis process. The high-resolution TEM (HR-TEM) image in Figure 1(d) clearly demonstrated that lattice fringes separated by 0.257 and 0.214 nm were observed, which correspond to the (002) plane of CuO and (200) plane of Cu_2O, respectively [40]. The selected area electron diffraction (SAED) pattern shown in Figure 1(e) also confirmed the existence of highly crystalline CuO and Cu_2O in CuO_x/Cu-PS1 microspheres [41]. The XRD pattern of CuO_x/Cu-PS1 microspheres is shown in Figure S1 (Supporting Information), and peaks of CuO (JCPDS, 44-0706) and Cu_2O (JCPDS, 34-1354) were mainly observed. The small peak marked with a triangle corresponded to metallic Cu (JCPDS, 04-0836) [41, 42]. It was hard to distinguish the lattice fringe and spot diffraction pattern of metallic copper because of its small crystal size, as shown in the XRD pattern of CuO_x/Cu-PS1 microspheres. The elemental mapping images shown in Figure 1(f) indicated uniformly distributed Cu and O elements over the hollow microsphere.

The crystal structures of composite microspheres synthesized as comparative samples are also shown in Figure S1. The XRD patterns of CuO_x/Cu-PS3 and CuO_x/Cu-PS5 microspheres showed that as more PS nanobeads decomposed,

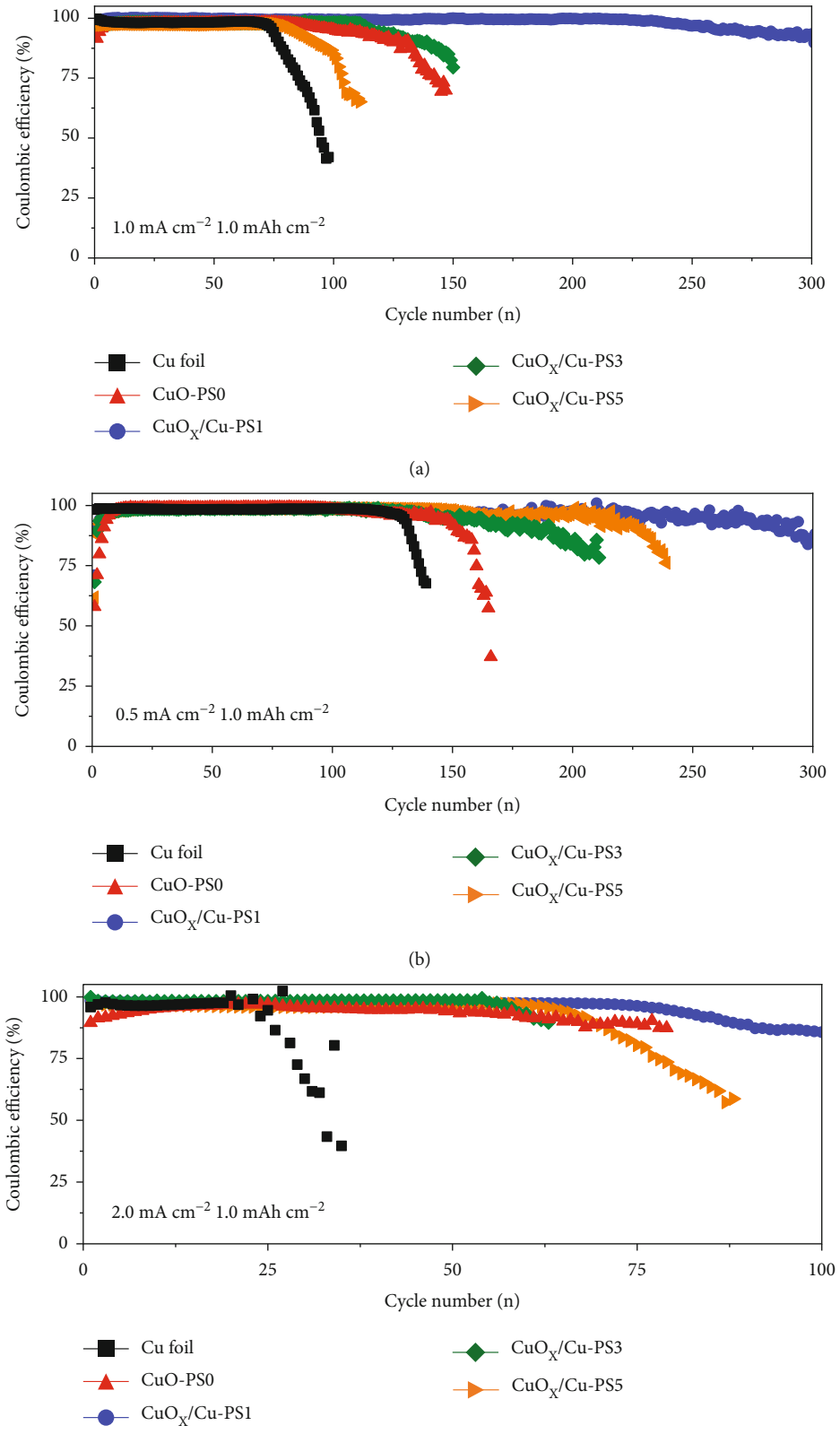

Figure 3: Continued.

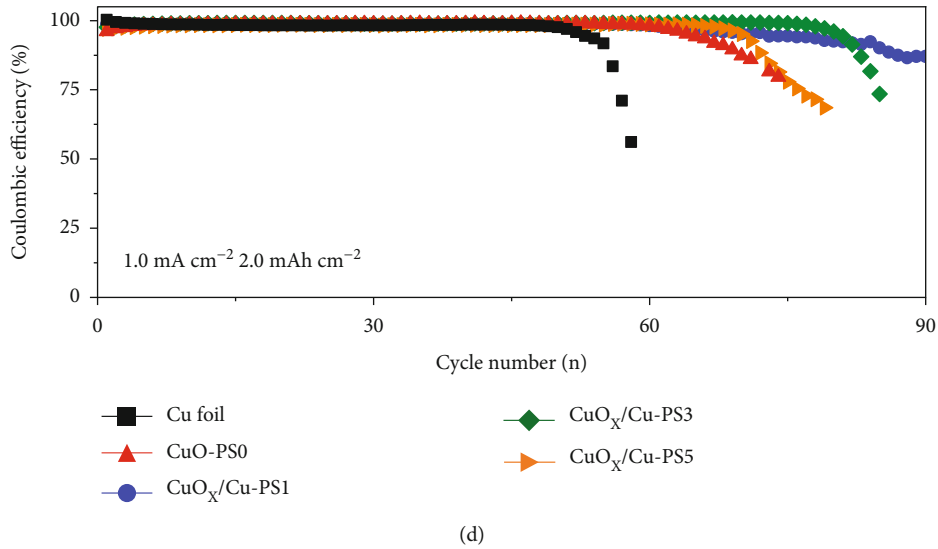

Figure 3: Coulombic efficiencies of bare Cu foil and CuO_x/Cu composite microspheres during plating and stripping of lithium at different current densities with different areal capacity: (a) 1.0 mA cm^{-2}, (b) 0.5 mA cm^{-2}, and (c) 2.0 mA cm^{-2} with 1.0 mAh cm^{-2} areal capacity of lithium and (d) 1.0 mA cm^{-2} with 2.0 mAh cm^{-2} areal capacity of lithium.

further reduction of CuO and Cu_2O progressed; therefore, sharp peaks of metallic copper were mainly observed. The only difference between the XRD patterns of CuO_x/Cu-PS3 and CuO_x/Cu-PS5 microspheres was the existence of CuO-related peaks, which are denoted with a square. The other comparative sample made without PS nanobeads was only composed of CuO crystals; therefore, it was denoted as CuO-PS0. The SEM and low-resolution TEM images of CuO_x/Cu-PS3 and CuO_x/Cu-PS5 microspheres in Figure S2A-C and Figure S3A-C, respectively, revealed comparatively dense structure covered with a larger crystal size of metallic copper than those of CuO_x/Cu-PS1 microspheres. As CuO_x/Cu-PS3 and CuO_x/Cu-PS5 microspheres experienced more PS nanobead decomposition during the spray pyrolysis process, sintering of metallic copper through mesopores from PS nanobeads was highly progressed, resulting in a dense structure. Three different lattice fringes separated by 0.253, 0.243, and 0.209 nm were discovered in the HR-TEM image of CuO_x/Cu-PS3 microspheres in Figure S2D, and these lattice fringes were matched well with (002) plane of CuO, (111) plane of Cu_2O, and (111) plane of Cu, respectively [43]. The SAED pattern of CuO_x/Cu-PS3 microspheres in Figure S2E also showed crystal planes of copper oxides and metallic copper. However, there was no CuO-related lattice fringe or SAED pattern for the CuO_x/Cu-PS5 microspheres, as shown in Figure S3D,E. As the CuO_x/Cu-PS5 microspheres underwent further reduction, fewer O elements were detected in elemental mapping images than those of CuO_x/Cu-PS3 microspheres and shown in Figure S2F and S3F. Morphological features of CuO-PS0 microspheres prepared without PS nanobeads were different from those of CuO_x/Cu-PS3 and CuO_x/Cu-PS5 microspheres, as shown in Figure S4A-C. SEM and low-resolution TEM images in Figure S4A-C indicated that CuO-PS0 microspheres were hollow microspheres composed of nanoparticles that were smaller than those of CuO_x/Cu-PS1 microspheres. The HR-TEM images and SAED patterns of CuO-PS0 microspheres in Figure S4D,E represented lattice fringes and SAED pattern rings of CuO phase. The elemental mapping images of CuO-PS0 microspheres also revealed hollow structure of composite microsphere.

The surface chemical states of CuO_x/Cu-PS1 microspheres and their comparative samples were investigated through XPS, shown in Figures 2(a) and 2(b) and Figure S5, respectively. The Cu 2p spectrum could be deconvoluted into peaks of Cu/Cu^+, peaks of Cu^{2+}, and Cu^{2+} satellite peaks [44]. The peaks at binding energies of 932.8 and 952.5 eV were attributed to $2p_{3/2}$ and $2p_{1/2}$ of Cu/Cu^+ oxidation states of copper, and the peaks at binding energies of 934.1 and 954.0 were ascribed to $2p_{3/2}$ and $2p_{1/2}$ of Cu^{2+} oxidation states of copper, respectively [42, 44, 45]. Comparing the deconvoluted regions of Cu/Cu^+-related peaks and Cu^{2+}-related peaks, the proportion of Cu^{2+}-related peaks decreased as the amount of PS nanobeads in the precursor solution increased. The three peaks at approximately 942.0 eV and a single peak at 961.8 eV corresponded to satellite peaks of Cu^{2+} [44].

The TGA data of CuO_x/Cu composite microspheres were acquired under an air atmosphere with a heating rate of 10°C per minute until reaching 800°C, as shown in Figure 2(c). Assuming the full transformation of Cu_2O and Cu to CuO, the samples containing Cu_2O or Cu should increase in weight during the analysis. However, CuO-PS0 microspheres, which were composed of CuO, lost a small amount of weight ascribed to the evaporation of adsorbed water molecules on their surface. The weight of CuO_x/Cu-PS1 microspheres was increased by 3% after the oxidation, and the weight percent of Cu_2O in CuO_x/Cu-PS1 microspheres was calculated at 3.7%, ignoring the small amount of metallic copper. In the case of CuO_x/Cu-PS5 microspheres, which were composed of Cu_2O and Cu crystals,

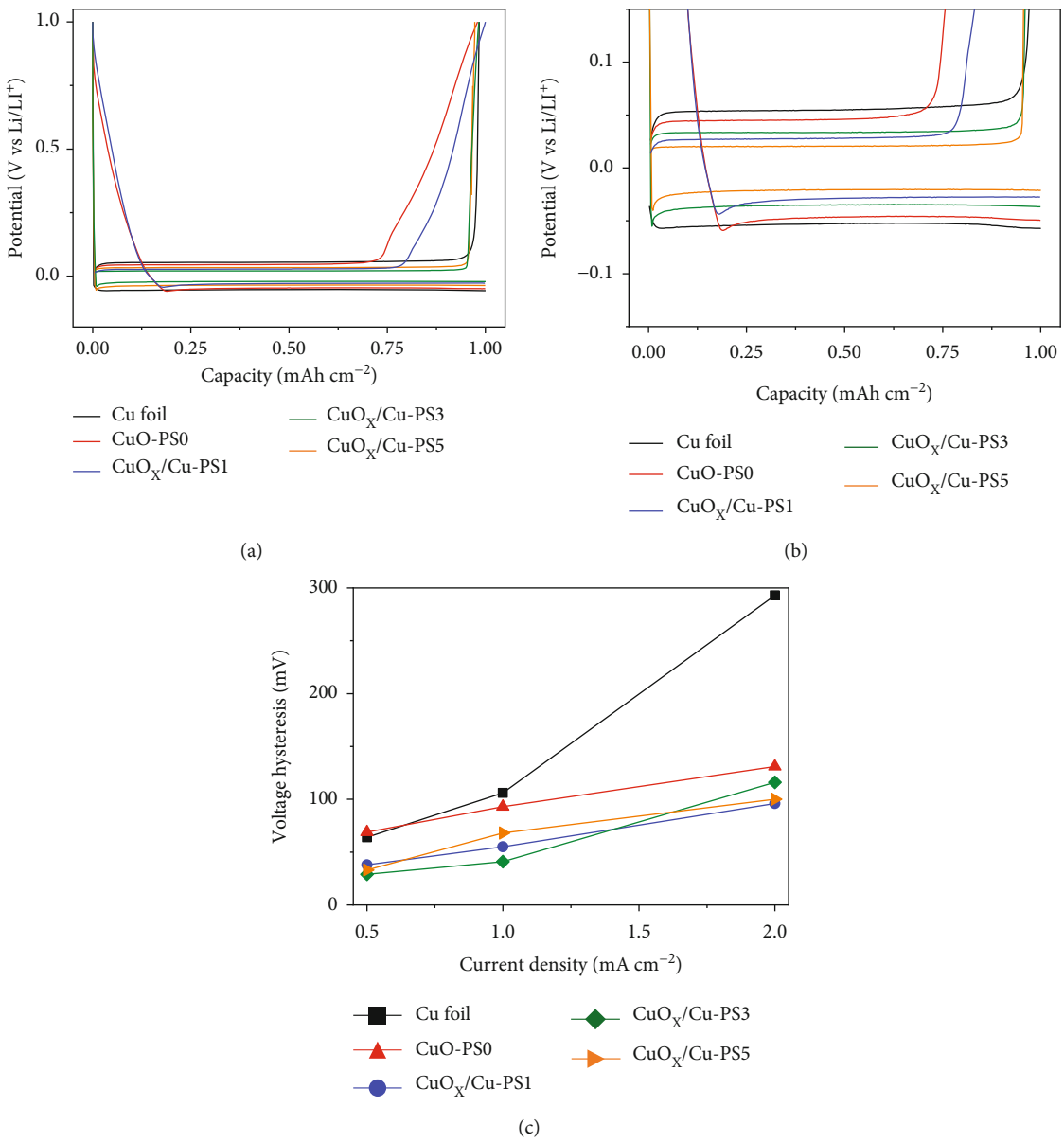

Figure 4: (a) Charge and discharge voltage profiles of the bare Cu foil and CuO_x/Cu composite microspheres at the current density of 1.0 mA cm^{-2} with the capacity of 1.0 mAh cm^{-2}, (b) enlarged image, and (c) voltage hysteresis of the bare Cu foil and CuO_x/Cu composite microspheres at the different current densities.

20% of the increased weight could be attributed to the transformation of 37.1% of Cu_2O and 62.9% of Cu to CuO. Figure 2(d) and Figure S6 demonstrate the Barrett-Joyner-Halenda (BJH) pore size distributions and the isotherm curves of N_2 gas adsorption and desorption of CuO_x/Cu composite microspheres, respectively. The Brunauer-Emmett-Teller (BET) surface areas of CuO_x/Cu-PS1, CuO_x/Cu-PS3, CuO_x/Cu-PS5, and CuO-PS0 microspheres were 13.1, 5.8, 6.0, and 18.6 $m^2 g^{-1}$, respectively, as shown in Figure 2(d) [46]. As shown in Figure S6, all microspheres showed type III isotherm, representing a macroporous structure [2]. The surface area of the samples decreased as the amount of PS nanobeads increased because sintering induced by the decomposition of PS nanobeads caused crystal growth inside the hollow microspheres. In particular, the surface area of CuO_x/Cu-PS3 and CuO_x/Cu-PS5 microspheres significantly decreased that they showed a dense structure, while CuO_x/Cu-PS1 and CuO-PS0 microspheres showed a hollow structure.

The Li plating/stripping behavior of CuO_x/Cu composite microspheres was estimated in a half-cell using lithium foil as the counter electrode. Coulombic efficiency (CE), which can be defined as capacity ratio of plated lithium and stripped lithium, is a crucial factor for evaluating the reversibility of repeated lithium plating and stripping processes [47, 48]. When the dendritic growth of lithium occurs during the cycles, lithium dendrites are wrapped by SEI films, making them electrochemically inert to current collectors and electrons, and are referred to as "dead lithium" [49, 50]. As the side reactions for SEI films consume electrolytes,

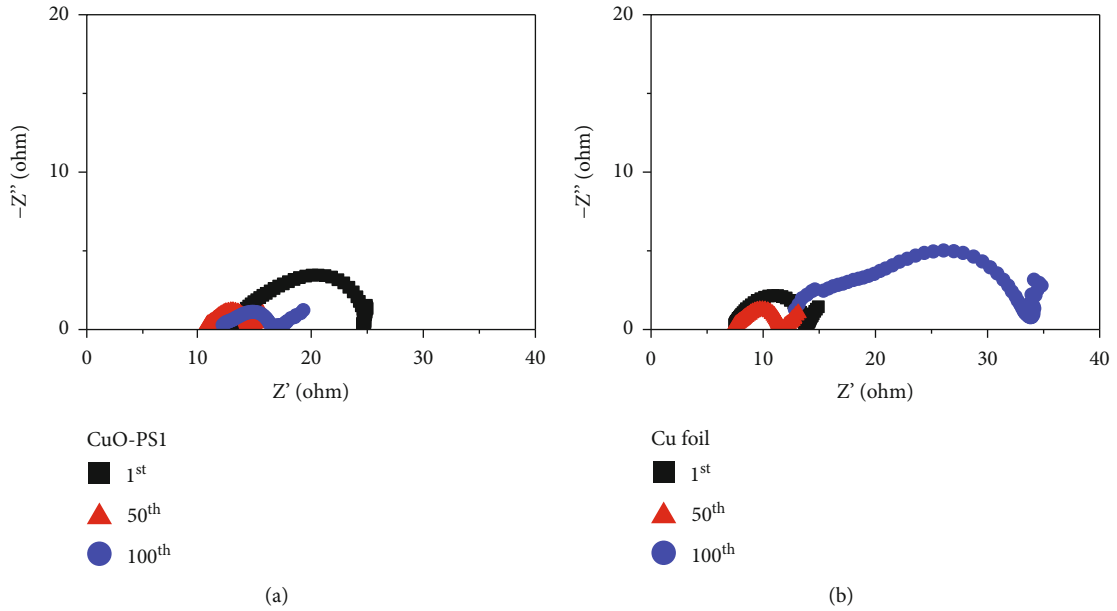

FIGURE 5: Nyquist plots of the impedance spectra of the asymmetric cells after 1st, 50th, and 100th cycles at the current density of 1.0 mA cm^{-2}: (a) CuO_x/Cu-PS1 microsphere and (b) bare Cu foil.

dead lithium decreases CE [49, 50]. Figures 3(a)–3(c) show the CEs of Cu foil and CuO_x/Cu composite microspheres at a specified current density (1.0, 0.5, and 2.0 mA cm^{-2}) with a fixed lithium deposition capacity of 1.0 mAh cm^{-2}. At a current density of 1.0 mA cm^{-2}, Cu foil maintained CE up to 98% for 70 cycles; subsequently, CE drastically decreased even under 40%, and the cell died before 100 cycles, as shown in Figure 3(a). This sudden failure of the cell during cycling could be attributed to an internal short circuit caused by dendritic lithium growth [51]. When CuO_x/Cu-PS3, CuO_x/Cu-PS5, and CuO-PS0 microspheres were used as host materials for lithium plating and tested at a current density of 1.0 mA cm^{-2}, the composite microspheres showed high CEs more than 98%. The CuO_x/Cu-PS3, CuO_x/Cu-PS5, and CuO-PS0 microspheres could reversibly keep their CE about 110, 80, and 90 cycles, respectively. The CuO_x/Cu-PS1 microspheres, conversely, demonstrated more than 99% of CEs for 220 cycles and decreased to 92% at the 300th cycle. At current density of 0.5 and 2.0 mA cm^{-2}, the CuO_x/Cu-PS1 microspheres exhibited higher CEs for longer cycles compared to Cu foil, CuO_x/Cu-PS3, CuO_x/Cu-PS5, and CuO-PS0 electrodes, as shown in Figures 3(b) and 3(c). In particular, the CuO_x/Cu-PS1 microspheres exhibited CEs of above 97% for more than 70 cycles at a high current density of 2.0 mA cm^{-2}. Furthermore, the CEs of Cu foil and CuO_x/Cu composite microspheres were also measured at higher capacity of 2.0 mAh cm^{-2} at the current density of 1.0 mA cm^{-2}, as demonstrated in Figure 3(d). Even though the amount of plated and deposited lithium was doubled, the composite microspheres showed more than 98% of CEs for more than 60 cycles.

Superior reversibility during the repeated deposition and stripping of lithium was confirmed through asymmetric coulombic efficiency tests. However, the reasons why CuO_x/Cu-PS1 microspheres exhibited better electrochemical performances should be investigated through other analyses. Therefore, voltage profiles of electrodes during the deposition and stripping of lithium at different current densities are studied and shown in Figure 4 and Figure S7. Figures 4(a) and 4(b) show voltage profiles of Cu foil and CuO_x/Cu composite microspheres under the condition of the current density of 1.0 mA cm^{-2} at the capacity of 1.0 mAh cm^{-2}. As shown in Figure 4(a), voltage profiles of CuO_x/Cu-PS1 and CuO-PS0 microspheres were different from the others that potential was linearly decreased due to the lithiation process of copper oxides [40, 52]. In contrast, electrodes with high contents of copper showed vertical drops of potential prior to the lithium plating process. The lithium nucleation overpotential, defined as the potential barrier for lithium to be deposited on the surface of materials, could be calculated by the voltage difference between and flat part of the voltage plateau during lithium deposition [53, 54]. The lithium nucleation overpotential on the CuO-PS0, CuO_x/Cu-PS1, CuO_x/Cu-PS3, and CuO_x/Cu-PS5 electrodes was calculated to 10.2, 12.0, 24.8, and 22.1 mV, respectively, as shown in Figure 4(b). These results indicated that higher contents of copper oxide can reduce the energy barrier for uniform deposition of lithium during the plating process. This might be ascribed to lithiophilic Li_2O generation during the lithiation process according to the conversion reaction of CuO_x/Cu-PS1 and CuO-PS0 microspheres, resulting in lower onset potential [40]. Voltage hysteresis in LMAs refers to the difference in potential between the plating and stripping voltage profiles of the anode that can affect the performance and CE of the battery [55]. The values of voltage hysteresis of the samples at different current densities are shown in Figure 4(c). CuO_x/Cu-PS3 and CuO_x/Cu-PS5 microspheres exhibited 29 and 33 mV of voltage hysteresis at a current density of 0.5 mA cm^{-2}, respectively, which were the lowest values among the samples due to the high

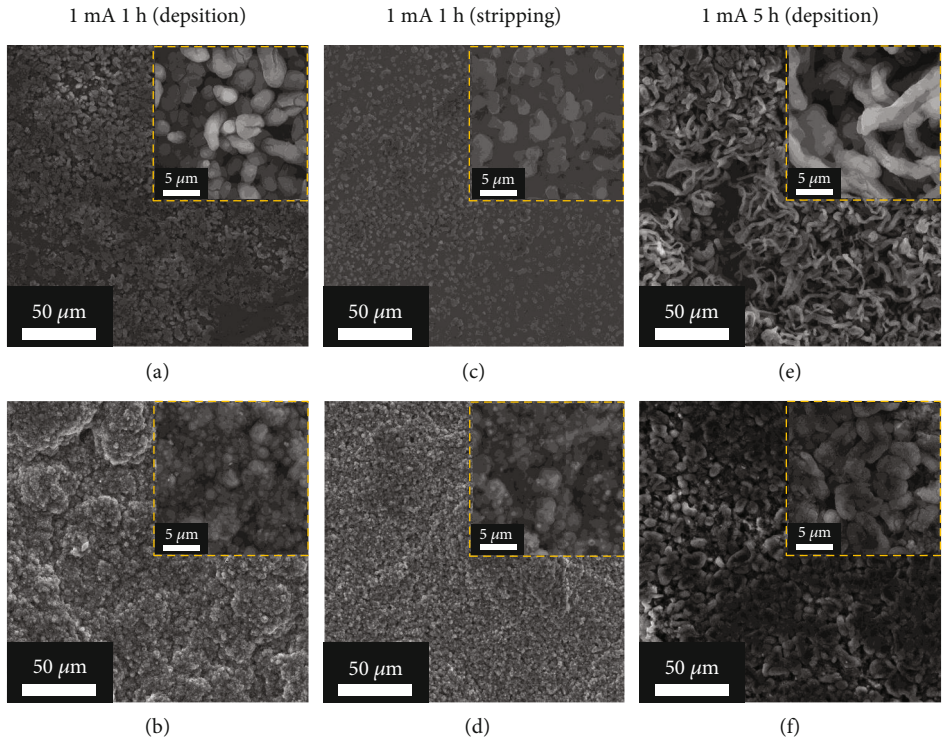

Figure 6: SEM images of (a, c, e) bare Cu foil and (b, d, f) CuO_x/Cu-PS1 microsphere: (a, b) after lithium plating 1.0 mAh cm^{-2}, (c, d) stripping 1.0 mAh cm^{-2} of lithium from the anode, and (e, f) after lithium plating 5.0 mAh cm^{-2}.

contents of metallic copper with high electrical conductivity, which can enhance electron transfer. CuO-PS0 microspheres exhibited 69 mV of voltage hysteresis and showed the largest value that could be attributed to the thick Li_2O SEI layer, which deteriorates the transportation of lithium ions and lowers the electrical conductivity of copper oxide [56–58]. However, as the current density increased to 2.0 mA cm^{-2}, the voltage hysteresis of CuO_x/Cu-PS3 and CuO_x/Cu-PS5 microspheres was increased to 116 and 100 mV, respectively. Lower contents of copper oxides at CuO_x/Cu-PS3 and CuO_x/Cu-PS5 microspheres led to fewer active sites on the surface of the structures and resulted in bulk lithium formation at high current densities [59]. However, the voltage hysteresis of CuO_x/Cu-PS1 microspheres increased from 38 mV to 95 mV when the current density was increased from 0.5 to 2.0 mA cm^{-2}. Owing to the lithiophilic and conductive nature of CuO_x/Cu-PS1 microspheres, sufficient nucleation sites of lithium and fast kinetics for lithium ion transport could be achieved with CuO_x/Cu-PS1 microspheres and resulted in a reduction of local current density and uniform and reversible lithium plating and stripping [60, 61].

The overpotential is deeply related to total impedance of the cell; therefore, in order to further comprehend the electrochemical performances of Cu foil and CuO_x/Cu composite microspheres, electrochemical impedance spectroscopy (EIS) of asymmetric cells was performed, as shown in Figure 5 and Figure S8. The EIS analysis was based on the equivalent circuit model shown in Figure S9. The Nyquist curves have one semicircle for cells after the first cycle and two semicircles for more cycled cells [17, 62, 63]. For the cells after the first cycle, the single semicircle is related to interfacial resistance, and low interfacial resistance indicates faster kinetics at the interface of electrolyte and electrode [64]. Comparing the interfacial resistance through the Nyquist curves of the first cycle, Cu foil, CuO_x/Cu-PS1, CuO_x/Cu-PS3, CuO_x/Cu-PS5, and CuO-PS0 electrodes showed 6.5, 11.7, 20.4, 20.7, and 16.0 Ω, respectively. Among the composite microspheres, CuO_x/Cu-PS1 and CuO-PS0 microspheres that composed of copper oxides showed lower interfacial resistance after the first cycle because of Li_2O generated from lithiation of copper oxide (Figure 5(a) and Figure S8A). As the cycles progressed, the total resistance of the cells reduced as the number of active sites at the surface of the electrodes increased. For the cycled cells, the Nyquist curves comprised two semicircles corresponding to the electrolyte and SEI resistance for the high-frequency region and charge-transfer resistance for medium-frequency range [62, 63]. After 100 cycles, except for the CuO_x/Cu-PS1 microspheres, the impedance of the cells was highly increased. As shown in Figure 5(b), the sum of the electrolyte resistance and charge-transfer resistance of Cu foil was 4.5 Ω at 50th cycle, which, however, increased to 21.1 Ω at the 100th cycle. The CuO_x/Cu-PS3, CuO_x/Cu-PS5, and CuO-PS0 microspheres also showed increased impedance from 4.4, 5.8, and 5.6 Ω to 8.1, 11.5, and 13.8 Ω, respectively (Figure S8). The Nyquist plots of CuO_x/Cu-PS3 and CuO_x/Cu-PS5 microspheres began at a resistance greater than 30 Ω, indicating that the samples had a high electrolyte resistance. As explained above, when dead lithium was generated during the cycles, newly deposited lithium reacted with the electrolyte and

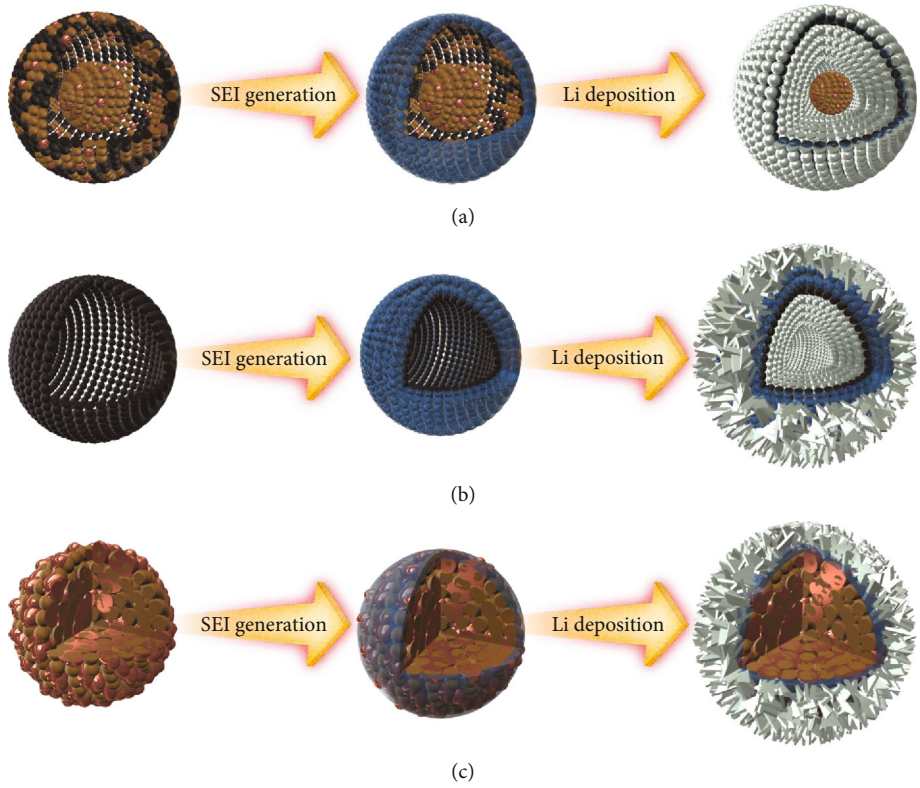

Scheme 2: Schematic illustrations of formation of SEI layer and lithium deposition behaviors of (a) CuO_x/Cu-PS1, (b) CuO-PS0, and (c) CuO_x/Cu-PS5 microsphere.

led to an increase in electrolyte resistance [62, 63]. The resistance of CuO_x/Cu-PS1 microspheres only increased 0.8 Ω from 50th cycle to 100th cycle, indicating uniform lithium deposition and cycling stability.

SEM images were recorded to investigate the plating and stripping behavior of lithium when Cu foil and CuO_x/Cu composite microspheres were used as electrodes at the current density of 1.0 mA cm^{-2}, as shown in Figure 6 and Figure S10. Lithium deposited on Cu foil with a capacity of 1.0 mAh cm^{-2}, and a current density of 1.0 mA cm^{-2} showed oval lithium grains. Their size was approximately 5.0 μm (Figure 6(a)). Figure 6(b) shows the SEM images of lithium deposited on CuO_x/Cu-PS1 microspheres under the same condition, and the surface of CuO_x/Cu-PS1 microspheres became as thick as the lithium and SEI films. Furthermore, lithium was encapsulated in the void space of CuO_x/Cu-PS1 microspheres, as shown in magnified SEM image in Figure 6(b). After lithium stripping, residual lithium grains remained on the surface of Cu foil (Figure 6(c)). The morphology of the CuO_x/Cu-PS1 microspheres was the same even after lithium stripping, except for the void space of CuO_x/Cu-PS1 microspheres, which was clearly observed, indicating reversible lithium deposition/stripping behavior. In the case of CuO-PS0 microspheres, hierarchically deposited lithium was visible on the surface, which was attributed to the thick SEI layer that impeded uniform lithium deposition (Figure S10A) [65]. After lithium stripping, the thick SEI layer on the surface of CuO-PS0 microspheres was clearly observed, as seen in Figure S10D. Lithium plating and stripping behavior on the CuO_x/Cu-PS3 and CuO_x/Cu-PS5 microspheres were similar. A thick SEI layer was covered around the microspheres, and bare lithium clusters were shown on the surface of the electrode surface as marked by dashed lines (Figure S10B,C). Because of the dense structure of CuO_x/Cu-PS3 and CuO_x/Cu-PS5 microspheres, the amount of lithium stored was limited, and residual lithium was deposited on the surface of the electrode. The SEM images of CuO_x/Cu-PS3 and CuO_x/Cu-PS5 microspheres after plating of lithium also showed remaining lithium clusters, and a thick SEI layer was covered all around the microspheres. Furthermore, lithium deposition at a capacity of 5.0 mAh cm^{-2} and a current density of 1.0 mA cm^{-2} was examined for practical applications. After plating of 5.0 mAh cm^{-2}, many dendrites were observed on Cu foil, as shown in Figure 6(e). This dendritic growth of lithium increased the impedance of the cell and consumed electrolytes and caused the early failure of cell. On the contrary, the SEM images of lithium plating of 5.0 mAh cm^{-2} on CuO_x/Cu-PS1 microspheres displayed no dendrites, as shown in Figure 6(f). After the void space of CuO_x/Cu-PS1 microspheres was fully filled, lithium was deposited on the surface of CuO_x/Cu-PS1 microspheres. Subsequently, more lithium deposition formed clusters of CuO_x/Cu-PS1 microspheres covered by lithium. The SEM images of CuO-PS0 microspheres after lithium plating of 5.0 mAh cm^{-2} displayed similar feature to those of CuO_x/Cu-PS1 microspheres as shown in Figure S10G. The 3D structure of CuO-PS0 microspheres was not found;

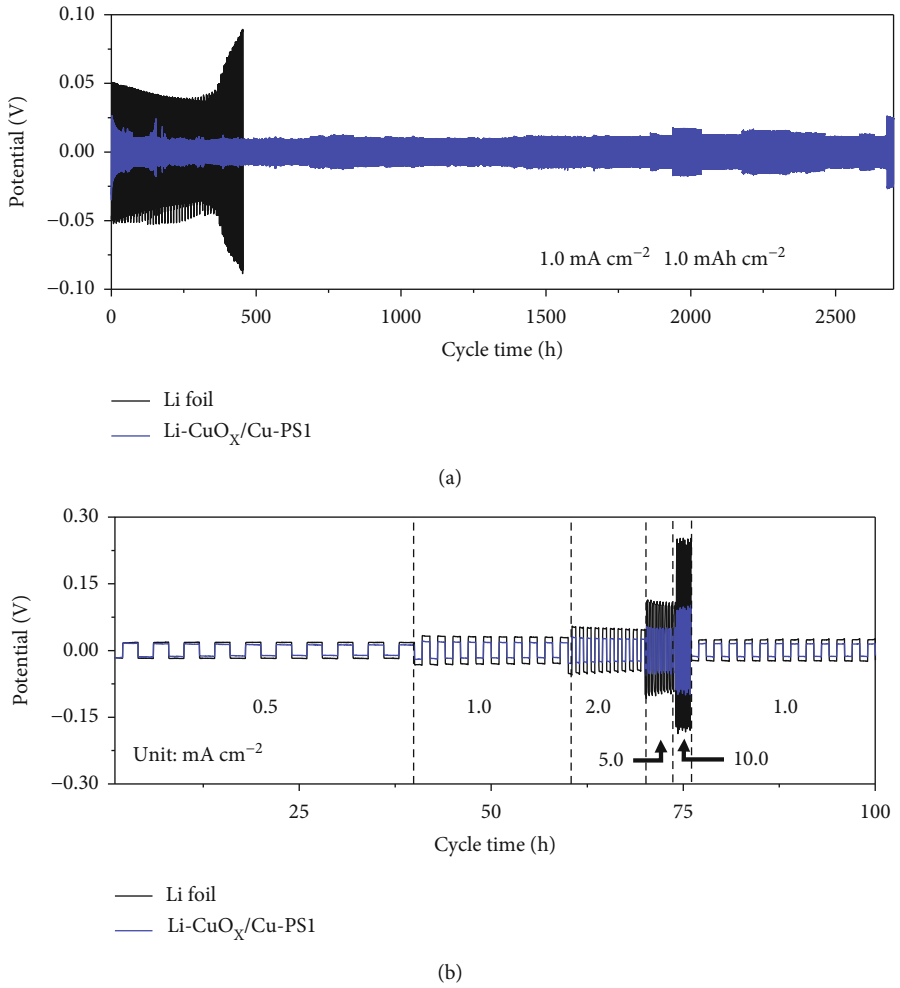

Figure 7: (a) Cycling performances of bare Li foil and Li-CuO_x/Cu-PS1 in a symmetrical cell test at 1.0 mA cm^{-2} with 1.0 mAh cm^{-2} and (b) rate performance of symmetric cells measured at current densities ranging from 0.5 to 10.0 mA for a capacity of 1.0 mAh cm^{-2}.

however, comparatively flat and dense lithium deposition was achieved. In the case of CuO_x/Cu-PS3 and CuO_x/Cu-PS5 microspheres (Figure S10H,I), only bulk lithium grains were observed, and some dendrites were also shown. In terms of the above results, lithium plating behaviors on composite microspheres are illustrated in Scheme 2.

Symmetric cells were tested to evaluate the long-term stability of the cells upon repeated lithium plating and stripping. Before the test, CuO_x/Cu composite microspheres as host materials were preplated with a capacity of 5.0 mAh cm^{-2} of lithium to form Li-CuO_x/Cu electrodes. Figure 7(a) shows the galvanostatic lithium plating and stripping profiles of symmetric cells obtained at a current density of 1.0 mA cm^{-2} with 1.0 mAh cm^{-2} for bare lithium foil and Li-CuO_x/Cu-PS1. Li-CuO_x/Cu-PS1 electrodes exhibited a stable voltage hysteresis of less than 20 mV over 2,500 h. On the contrary, the symmetric cell made of bare lithium foil showed 80 mV of voltage hysteresis at 300 h; subsequently, voltage hysteresis gradually increased, and the cell failed at 450 h. Figure 7(b) and Figure S11 show voltage-time profiles of the galvanostatic cycling test of symmetric cells estimated at a fixed capacity of 1.0 mAh cm^{-2} under an increasing current density from 0.5 to 10.0 mA cm^{-2}. At the low current density of 0.5 mA cm^{-2}, Li foil, Li-CuO_x/Cu-PS1, Li-CuO-PS0, Li-CuO_x/Cu-PS3, and Li-CuO_x/Cu-PS5 electrodes exhibited low voltage hysteresis of 36, 22, 21, 24, and 39 mV, respectively. However, as the current densities increased, the voltage hysteresis of Li foil, Li-CuO_x/Cu-PS3, and Li-CuO_x/Cu-PS5 electrodes highly increased compared to those of the Li-CuO_x/Cu-PS1 and Li-CuO-PS0 electrodes. For instance, the voltage hysteresis values of the Li-CuO_x/Cu-PS1 were 22, 32, 48, 95, 196, and 28 mV at the current densities of 0.5, 1.0, 2.0, 5.0, 10.0, and 1.0 mA cm^{-2}, respectively. However, the voltage hysteresis values of lithium foil were 36, 58, 98, 203, 431, and 48 mV at the current densities of 0.5, 1.0, 2.0, 5.0, 10.0, and 1.0 mA cm^{-2}. These results indicated that the Li-CuO_x/Cu-PS1 electrodes showed stable and reversible lithium plating and stripping behaviors even at a high current density. Li-CuO-PS0 electrodes also exhibited excellent symmetric cell performances; however, Li-CuO_x/Cu-PS3 and Li-CuO_x/Cu-PS5 electrodes showed worse symmetric cell performances than lithium foil that at the current density of 10.0 mA cm^{-2}, their voltage profiles were unstable. When the current density went back to 1.0 mA cm^{-2}, the cells experienced short circuit and failed. These results matched well with lithium deposition SEM images of Figure 6 and Figure S10. Figure S11B displays

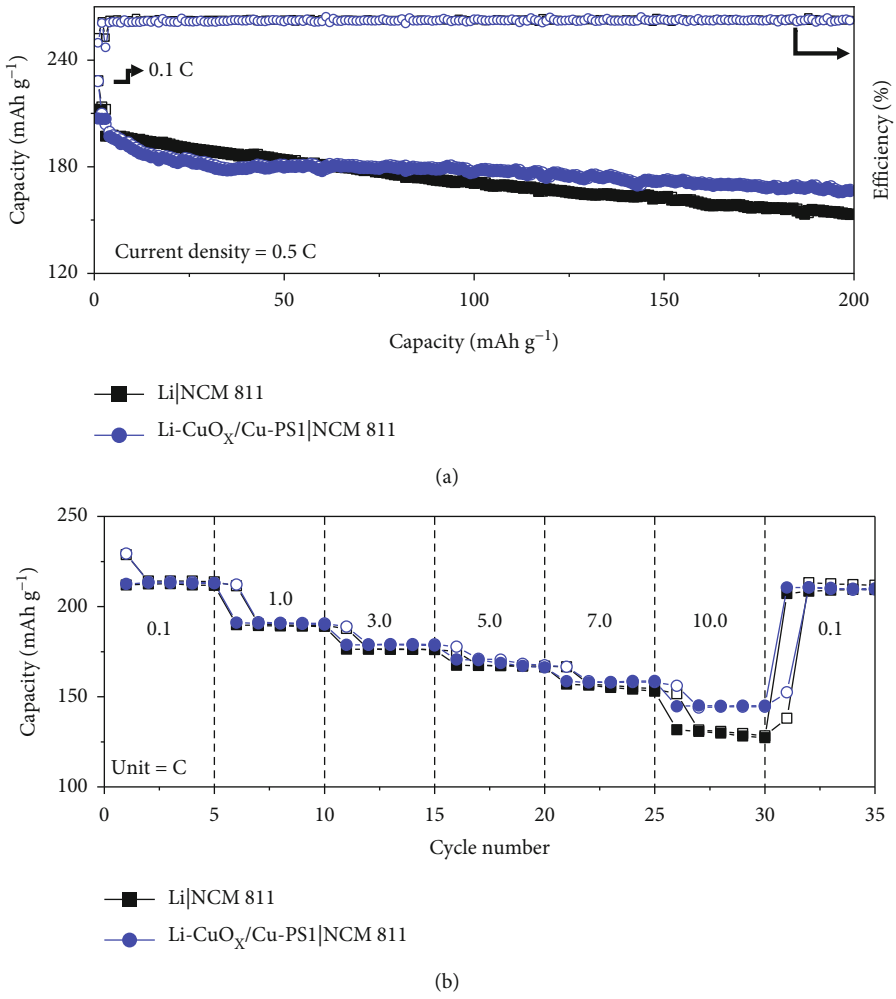

Figure 8: (a) Cycling performances at a current density of 0.5 C and (b) rate capability at increasing current densities from 0.1 to 10.0 C for Li|NCM 811 and Li-CuO_x/Cu-PS1|NCM 811 full cells.

voltage-time profiles of symmetrical cells of Li-CuO_x/Cu-PS1 electrodes and bare lithium foil at the same current density of 1.0 mA cm^{-2} with higher capacity of 2.0 mAh cm^{-2}. Even at the higher capacity condition, Li-CuO_x/Cu-PS1 electrodes exhibited low voltage hysteresis of 35 mV more than 500 h. On the other hand, symmetrical cell based on bare lithium foil showed a lower voltage hysteresis of 26 mV until 160 h; however, this voltage hysteresis gradually increased, and the cell failed after 220 h.

To demonstrate the practical application of CuO_x/Cu-PS1 microspheres as host materials for LMAs, a full cell was assembled with Li-CuO_x/Cu-PS1 and bare lithium foil as the anode and $LiNi_{0.8}Co_{0.1}Mn_{0.1}O_2$ (NCM 811) as the cathode. The assembled full cells were denoted as Li-CuO_x/Cu-PS1|NCM 811 and Li|NCM 811. The electrochemical properties of Li-CuO_x/Cu-PS1|NCM 811 and Li|NCM 811 with a cut-off potential range of 2.5-4.3 V are shown in Figure 8. Figure 8(a) illustrates the cycling performances of Li-CuO_x/Cu-PS1|NCM 811 and Li|NCM 811 at the current density of 0.5C (1 C = 200 mAh g^{-1}), and Li-CuO_x/Cu-PS1|NCM 811 exhibited better cycling stability that the cell has capacity retention of 81.6% after 200 cycles. The improved electrochemical performance through introducing CuO_x/Cu-PS1 microspheres as a host material for lithium storage was further proved by the rate capability test at increased current densities ranging from 0.1 to 10.0 C (Figure 8(b)). The reversible discharge capacities of Li-CuO_x/Cu-PS1|NCM 811 were 213.0, 190.6, 179.0, 167.3, 158.1, and 144.5 mAh g^{-1} at current densities of 0.1, 1.0, 3.0, 5.0, 7.0, and 10.0 C, respectively. However, the reversible discharge capacities of Li|NCM 811 were 213.7, 189.4, 176.3, 166.9, 154.3, and 128.3 mAh g^{-1} at current densities of 0.1, 1.0, 3.0, 5.0, 7.0, and 10.0 C, respectively. As the current densities increased, the capacity gap between Li-CuO_x/Cu-PS1|NCM 811 and Li|NCM 811 widened, indicating a better rate performance of Li-CuO_x/Cu-PS1|NCM 811 cell. Enhanced electrochemical properties of Li-CuO_x/Cu-PS1|NCM 811 also could be identified through the galvanostatic charge-discharge profiles of the cells at increased current densities, as shown in Figure S12. At a low current density of 0.1 C (Figure S12A), charge-discharge profiles of Li-CuO_x/Cu-PS1|NCM 811 and Li|NCM 811 were reasonably consistent with each other. On the other hand, as the current densities were increased to 5.0, 7.0, and 10.0 C, Li-CuO_x/Cu-PS1|NCM 811 showed

lower voltage hysteresis than those of Li|NCM 811, as shown in Figure S12B-D. The low voltage hysteresis indicated stable lithium plating and stripping features of Li-CuO_x/Cu-PS1 anode during the cycling of the full cell. The above results of Li-CuO_x/Cu-PS1|NCM 811 supported the idea that when CuOx/Cu-PS1 microspheres were used as host materials for practical full cell applications, the electrochemical performances of the cell could be improved due to the stable and reversible lithium plating and stripping behavior on CuO_x/Cu-PS1 microspheres.

4. Conclusions

In this study, a facile synthetic strategy for host material with a new composition of LMAs through one-step spray pyrolysis has been reported. During the spray pyrolysis process, the amount of PS nanobeads in the precursor solution affected to the ratio of CuO, Cu_2O, and Cu phases in the composite microspheres and pore structure. Optimization of the ratio between lithiophilic copper oxide and conductive metallic copper provided nucleation sites for lithium to be uniformly deposited and enhanced kinetics of lithium ions and electrons. Furthermore, the hollow structure of the microspheres offered void space for lithium to store lithium. Lithium deposited on the CuO_x/Cu-PS1 microspheres has a high CE of 99% at a current density of 1.0 mA cm^{-2} for more than 200 cycles. Moreover, the symmetrical cell of Li-CuO_x/Cu-PS1 electrodes exhibited more than 2,500 h, and full cell assembled with NCM 811 also showed better performances compared to bare lithium foil. This work illustrates a simple way for synthesizing host materials to achieve a uniform and reversible lithium deposition and stripping and controlling dendritic growth of lithium.

Data Availability

Data is available on request.

Conflicts of Interest

The authors declare that they have no conflicts of interest.

Acknowledgments

This research was supported by the National Research Council of Science & Technology (NST) grant by the Korea government (MSIT) (no. CAP22082-100) and the Ministry of Trade, Industry & Energy (MOTIE) of the Republic of Korea under grant no. 20011040. This research was supported by the National Research Foundation of Korea (NRF) grant funded by the Korea government (MSIT; no. 2021M3H4A3A02086430).

Supplementary Materials

Additional supporting information may be found online in the Supporting Information at the end of the article. Experimental Section (continued). Supplementary Figure S1: XRD patterns of CuO_x/Cu composite microspheres. Supplementary Figure S2: morphologies of CuO_x/Cu-PS3 microsphere synthesized through spray pyrolysis process: (A) SEM image, (B, C) TEM images, (D) HR-TEM image, (E) SAED pattern, and (F) elemental mapping images. Supplementary Figure S3: morphologies of CuO_x/Cu-PS5 microsphere synthesized through spray pyrolysis process: (A) SEM image, (B, C) TEM images, (D) HR-TEM image, (E) SAED pattern, and (F) elemental mapping images. Supplementary Figure S4: morphologies of CuO-PS0 microsphere synthesized through spray pyrolysis process: (A) SEM image, (B, C) TEM images, (D) HR-TEM image, (E) SAED pattern, and (F) elemental mapping images. Supplementary Figure S5: XPS spectra of (A, B) CuO-PS0, (C, D) CuO_x/Cu-PS3, and (E, F) CuO_x/Cu-PS5 microspheres: (A, C, E) Cu 2p and (B, D, F) O 1s. Supplementary Figure S6: N_2 adsorption and desorption isotherms of CuO_x/Cu composite microspheres. Supplementary Figure S7: charge and discharge voltage profiles of the bare Cu foil and CuO_x/Cu composite microspheres at the current density of (A, B) 0.5 mA cm^{-2} and (C, D) 2.0 mA cm^{-2} with the capacity of 1.0 mAh cm^{-2}. Supplementary Figure S8: Nyquist plots of the impedance spectra of the asymmetric cells after 1st, 50th, and 100th cycles at the current density of 1.0 mA cm^{-2}: (A) CuO_x/Cu-PS3, (B) CuO_x/Cu-PS5, and (C) CuO-PS0 microspheres. Supplementary Figure S9: equivalent circuit model used for AC impedance fitting. Supplementary Figure S10: SEM images of (A, D, G) CuO-PS0, (B, E, H) CuO_x/Cu-PS3, and (C, F, I) CuO_x/Cu-PS5 microsphere: (A–C) after lithium plating 1.0 mAh cm^{-2}, (D–F) stripping 1.0 mAh cm^{-2} of lithium from the anode, and (g, h, i) after lithium plating 5.0 mAh cm^{-2}. Supplementary Figure S11: (A) rate performance of Li-CuO-PS0, Li-CuO_x/Cu-PS3, and Li-CuO_x/Cu-PS5 in symmetrical cells measured at current densities ranging from 0.5 to 10.0 mA for a capacity of 1.0 mAh cm^{-2} and (B) cycling performance of bare Li foil and Li-CuO_x/Cu-PS1 in symmetrical cells measured at current densities of 1.0 mA cm^{-2} for a capacity of 2.0 mAh cm^{-2}. Supplementary Figure S12: charge and discharge voltage profiles of the Li|NCM 811 and Li-CuO_x/Cu-PS1|NCM 811 full cells at the current density of (A) 0.1 C, (B) 5.0 C, (C) 7.0 C, and (D) 10.0 C. *(Supplementary Materials)*

References

[1] J. Janek and W. G. Zeier, "A solid future for battery development," *Nature Energy*, vol. 1, no. 9, pp. 1–4, 2016.

[2] Q. Zhang, M.-L. Chen, J. Wang et al., "Ultrafine ZnSe/CoSe nanodots encapsulated in core–shell MOF-derived hierarchically porous N-doped carbon nanotubes for superior lithium/sodium storage," *Journal of Materials Chemistry A*, vol. 11, no. 10, pp. 5056–5066, 2023.

[3] W. Xu, J. Wang, F. Ding et al., "Lithium metal anodes for rechargeable batteries," *Energy & Environmental Science*, vol. 7, no. 2, pp. 513–537, 2014.

[4] Y. Sun, N. Liu, and Y. Cui, "Promises and challenges of nanomaterials for lithium-based rechargeable batteries," *Nature Energy*, vol. 1, no. 7, pp. 1–12, 2016.

[5] X.-B. Cheng and Q. Zhang, "Dendrite-free lithium metal anodes: stable solid electrolyte interphases for high-efficiency batteries," *Journal of Materials Chemistry A*, vol. 3, no. 14, pp. 7207–7209, 2015.

[6] P.-Y. Zhai, H.-J. Peng, X.-B. Cheng et al., "Scaled-up fabrication of porous-graphene-modified separators for high-capacity lithium-sulfur batteries," *Energy Storage Materials*, vol. 7, pp. 56–63, 2017.

[7] H. J. Peng, D. W. Wang, J. Q. Huang et al., "Janus separator of polypropylene-supported cellular graphene framework for sulfur cathodes with high utilization in lithium–sulfur batteries," *Advancement of Science*, vol. 3, no. 1, article 1500268, 2016.

[8] D. A. Dornbusch, R. Hilton, S. D. Lohman, and G. J. Suppes, "Experimental validation of the elimination of dendrite short-circuit failure in secondary lithium-metal convection cell batteries," *Journal of the Electrochemical Society*, vol. 162, no. 3, pp. A262–A268, 2015.

[9] H. Wang, Y. Liu, Y. Li, and Y. Cui, "Lithium metal anode materials design: interphase and host," *Electrochemical Energy Reviews*, vol. 2, no. 4, pp. 509–517, 2019.

[10] H. Zhuang, T. Zhang, H. Xiao et al., "3D Free-StandingCarbon nanofibers modified by lithiophilic metals EnablingDendrite-FreeAnodes for Li metal batteries," *Energy & Environmental Materials*, vol. 6, no. 3, article e12470, 2023.

[11] X.-B. Cheng, R. Zhang, C.-Z. Zhao, and Q. Zhang, "Toward safe lithium metal anode in rechargeable batteries: a review," *Chemical Reviews*, vol. 117, no. 15, pp. 10403–10473, 2017.

[12] D. Rehnlund, F. Lindgren, S. Böhme et al., "Lithium trapping in alloy forming electrodes and current collectors for lithium based batteries," *Energy & Environmental Science*, vol. 10, no. 6, pp. 1350–1357, 2017.

[13] L. Shi, A. Xu, and T. Zhao, "First-principles investigations of the working mechanism of 2D h-BN as an interfacial layer for the anode of lithium metal batteries," *ACS Applied Materials & Interfaces*, vol. 9, no. 2, pp. 1987–1994, 2017.

[14] G. Zheng, S. W. Lee, Z. Liang et al., "Interconnected hollow carbon nanospheres for stable lithium metal anodes," *Nature Nanotechnology*, vol. 9, no. 8, pp. 618–623, 2014.

[15] B. Zhu, Y. Jin, X. Hu et al., "Poly (dimethylsiloxane) thin film as a stable interfacial layer for high-performance lithium-metal battery anodes," *Advanced Materials*, vol. 29, no. 2, article 1603755, 2017.

[16] D. Ding, B. Zhang, L. Wang, J. Dou, Y. Zhai, and L. Xu, "Flexible Mg_3N_2 layer regulates lithium plating-striping for stable and high capacity lithium metal anodes," *Nano Research*, vol. 15, no. 9, pp. 8128–8135, 2022.

[17] D. Xie, Z. W. Wang, Z. Y. Gu et al., "Polymeric molecular design towards horizontal Zn electrodeposits at constrained 2D Zn2+diffusion: dendrite-free Zn anode for long-life and high-rate aqueous zinc metal battery," *Advanced Functional Materials*, vol. 32, no. 32, article 2204066, 2022.

[18] D. Xie, H.-H. Li, W.-Y. Diao et al., "Spatial confinement of vertical arrays of lithiophilic SnS_2 nanosheets enables conformal Li nucleation/growth towards dendrite-free Li metal anode," *Energy Storage Materials*, vol. 36, pp. 504–513, 2021.

[19] Y. Zhang, W. Luo, C. Wang et al., "High-capacity, low-tortuosity, and channel-guided lithium metal anode," *Proceedings of the National Academy of Sciences*, vol. 114, no. 14, pp. 3584–3589, 2017.

[20] K. Huang, S. Bi, B. Kurt et al., "Regulation of SEI formation by anion receptors to achieve ultra-stable lithium-metal batteries," *Angewandte Chemie International Edition*, vol. 133, no. 35, pp. 19381–19389, 2021.

[21] R. Zhang, N. W. Li, X. B. Cheng, Y. X. Yin, Q. Zhang, and Y. G. Guo, "Advanced micro/nanostructures for lithium metal anodes," *Advancement of Science*, vol. 4, no. 3, article 1600445, 2017.

[22] H. Wang, X. Cao, H. Gu et al., "Improving lithium metal composite anodes with seeding and pillaring effects of silicon nanoparticles," *ACS Nano*, vol. 14, no. 4, pp. 4601–4608, 2020.

[23] L. Yue, Y. Qi, Y. Niu, S. Bao, and M. Xu, "Low-barrier, dendrite-free, and stable Na plating/stripping enabled by gradient sodiophilic carbon skeleton," *Advanced Energy Materials*, vol. 11, no. 48, article 2102497, 2021.

[24] R. Akolkar, "Mathematical model of the dendritic growth during lithium electrodeposition," *Journal of Power Sources*, vol. 232, pp. 23–28, 2013.

[25] R. Zhang, X. B. Cheng, C. Z. Zhao et al., "Conductive nanostructured scaffolds render low local current density to inhibit lithium dendrite growth," *Advanced Materials*, vol. 28, no. 11, pp. 2155–2162, 2016.

[26] Z. Liang, G. Zheng, C. Liu et al., "Polymer nanofiber-guided uniform lithium deposition for battery electrodes," *Nano Letters*, vol. 15, no. 5, pp. 2910–2916, 2015.

[27] Z. Liang, D. Lin, J. Zhao et al., "Composite lithium metal anode by melt infusion of lithium into a 3D conducting scaffold with lithiophilic coating," *Proceedings of the National Academy of Sciences*, vol. 113, no. 11, pp. 2862–2867, 2016.

[28] Z. Luo, S. Li, L. Yang et al., "Interfacially redistributed charge for robust lithium metal anode," *Nano Energy*, vol. 87, article 106212, 2021.

[29] C.-P. Yang, Y.-X. Yin, S.-F. Zhang, N.-W. Li, and Y.-G. Guo, "Accommodating lithium into 3D current collectors with a submicron skeleton towards long-life lithium metal anodes," *Nature Communications*, vol. 6, no. 1, p. 8058, 2015.

[30] Q. Li, S. Zhu, and Y. Lu, "3D porous Cu current collector/Li-metal composite anode for stable lithium-metal batteries," *Advanced Functional Materials*, vol. 27, no. 18, article 1606422, 2017.

[31] S. Fang, D. Bresser, and S. Passerini, "Transition metal oxide anodes for electrochemical energy storage in lithium-and sodium-ion batteries," *Transition Metal Oxides for Electrochemical Energy Storage*, vol. 10, no. 1, pp. 55–99, 2022.

[32] P. Xue, C. Sun, H. Li, J. Liang, and C. Lai, "Superlithiophilic amorphous SiO_2–TiO_2 distributed into porous carbon skeleton enabling uniform lithium deposition for stable lithium metal batteries," *Advancement of Science*, vol. 6, no. 18, article 1900943, 2019.

[33] L. Ruan, X. Qin, K. Lin et al., "TiO_2/Cu_2O heterostructure enabling selective and uniform lithium deposition towards stable lithium metal anodes," *Nano Research*, vol. 16, no. 4, pp. 4917–4925, 2023.

[34] Y. Zhang, B. Liu, E. Hitz et al., "A carbon-based 3D current collector with surface protection for Li metal anode," *Nano Research*, vol. 10, no. 4, pp. 1356–1365, 2017.

[35] S. Matsuda, Y. Kubo, K. Uosaki, and S. Nakanishi, "Lithium-metal deposition/dissolution within internal space of CNT 3D matrix results in prolonged cycle of lithium-metal negative electrode," *Carbon*, vol. 119, pp. 119–123, 2017.

[36] H. Lee, J. Song, Y.-J. Kim, J.-K. Park, and H.-T. Kim, "Structural modulation of lithium metal-electrolyte interface with three-dimensional metallic interlayer for high-performance lithium metal batteries," *Scientific Reports*, vol. 6, no. 1, pp. 1–10, 2016.

[37] L.-L. Lu, J. Ge, J.-N. Yang et al., "Free-standing copper nanowire network current collector for improving lithium anode performance," *Nano Letters*, vol. 16, no. 7, pp. 4431–4437, 2016.

[38] T. Gonzalez-Carreno, M. Morales, M. Gracia, and C. Serna, "Preparation of uniform γ-Fe_2O_3 particles with nanometer size by spray pyrolysis," *Materials Letters*, vol. 18, no. 3, pp. 151–155, 1993.

[39] M. Yamukyan, K. V. Manukyan, and S. Kharatyan, "Copper oxide reduction by combined reducers under the combustion mode," *Chemical Engineering Journal*, vol. 137, no. 3, pp. 636–642, 2008.

[40] Y. Cai, B. Qin, C. Li et al., "A successive "conversion-deposition" mechanism achieved by micro-crystalline Cu_2O modified current collector for composite lithium anode," *Journal of Industrial and Engineering Chemistry*, vol. 120, pp. 285–292, 2023.

[41] Y. Cai, B. Qin, C. Li et al., "Stable lithium metal anode achieved by shortening diffusion path on solid electrolyte interface derived from Cu_2O lithiophilic layer," *Chemical Engineering Journal*, vol. 433, article 133689, 2022.

[42] Q. Zhang, J. Luan, Y. Tang, X. Ji, S. Wang, and H. Wang, "A facile annealing strategy for achieving in situ controllable Cu_2O nanoparticle decorated copper foil as a current collector for stable lithium metal anodes," *Journal of Materials Chemistry A*, vol. 6, no. 38, pp. 18444–18448, 2018.

[43] A. Sahai, N. Goswami, S. Kaushik, and S. Tripathi, "Cu/Cu_2O/CuO nanoparticles: novel synthesis by exploding wire technique and extensive characterization," *Applied Surface Science*, vol. 390, pp. 974–983, 2016.

[44] N. Pauly, S. Tougaard, and F. Yubero, "Determination of the Cu 2p primary excitation spectra for Cu, Cu_2O and CuO," *Surface Science*, vol. 620, pp. 17–22, 2014.

[45] A.-m. Cao, J. D. Monnell, C. Matranga, J.-m. Wu, L.-l. Cao, and D. Gao, "Hierarchical nanostructured copper oxide and its application in arsenic removal," *Journal of Physical Chemistry C*, vol. 111, no. 50, pp. 18624–18628, 2007.

[46] Y. Wang, Y. Lü, W. Zhan, Z. Xie, Q. Kuang, and L. Zheng, "Synthesis of porous Cu_2O/CuO cages using Cu-based metal–organic frameworks as templates and their gas-sensing properties," *Journal of Materials Chemistry A*, vol. 3, no. 24, pp. 12796–12803, 2015.

[47] J. Liu, Z. Bao, Y. Cui et al., "Pathways for practical high-energy long-cycling lithium metal batteries," *Nature Energy*, vol. 4, no. 3, pp. 180–186, 2019.

[48] Z. Li, M. Peng, X. Zhou et al., "In situ chemical lithiation transforms diamond-like carbon into an ultrastrong ion conductor for dendrite-free lithium-metal anodes," *Advanced Materials*, vol. 33, no. 37, article e2100793, 2021.

[49] A. Kushima, K. P. So, C. Su et al., "Liquid cell transmission electron microscopy observation of lithium metal growth and dissolution: root growth, dead lithium and lithium flotsams," *Nano Energy*, vol. 32, pp. 271–279, 2017.

[50] A. Aryanfar, D. J. Brooks, A. J. Colussi, and M. R. Hoffmann, "Quantifying the dependence of dead lithium losses on the cycling period in lithium metal batteries," *Physical Chemistry Chemical Physics*, vol. 16, no. 45, pp. 24965–24970, 2014.

[51] F. Sun, R. Moroni, K. Dong et al., "Study of the mechanisms of internal short circuit in a Li/Li cell by synchrotron X-ray phase contrast tomography," *ACS Energy Letters*, vol. 2, no. 1, pp. 94–104, 2017.

[52] G. Wang, X. Xiong, P. Zou et al., "Lithiated zinc oxide nanorod arrays on copper current collectors for robust Li metal anodes," *Chemical Engineering Journal*, vol. 378, article 122243, 2019.

[53] C. Wei, H. Fei, Y. An, Y. Tao, J. Feng, and Y. Qian, "Uniform Li deposition by regulating the initial nucleation barrier via a simple liquid-metal coating for a dendrite-free Li–metal anode," *Journal of Materials Chemistry A*, vol. 7, no. 32, pp. 18861–18870, 2019.

[54] R. Pathak, Y. Zhou, and Q. Qiao, "Recent advances in lithiophilic porous framework toward dendrite-free lithium metal anode," *Applied Sciences*, vol. 10, no. 12, p. 4185, 2020.

[55] S. S. Chi, Y. Liu, W. L. Song, L. Z. Fan, and Q. Zhang, "Prestoring lithium into stable 3D nickel foam host as dendrite-free lithium metal anode," *Advanced Functional Materials*, vol. 27, no. 24, article 1700348, 2017.

[56] Y. Xu, H. Wu, Y. He et al., "Atomic to nanoscale origin of vinylene carbonate enhanced cycling stability of lithium metal anode revealed by cryo-transmission electron microscopy," *Nano Letters*, vol. 20, no. 1, pp. 418–425, 2020.

[57] B. Han, Z. Zhang, Y. Zou et al., "Poor stability of Li_2CO_3 in the solid electrolyte interphase of a lithium-metal anode revealed by cryo-electron microscopy," *Advanced Materials*, vol. 33, no. 22, article e2100404, 2021.

[58] Z. Zhang, X. Xu, S. Wang et al., "Li_2O-reinforced Cu nanoclusters as porous structure for dendrite-free and long-lifespan lithium metal anode," *ACS Applied Materials & Interfaces*, vol. 8, no. 40, pp. 26801–26808, 2016.

[59] J. Luan, Q. Zhang, H. Yuan et al., "Plasma-strengthened lithiophilicity of copper oxide nanosheet–decorated Cu foil for stable lithium metal anode," *Advancement of Science*, vol. 6, no. 20, article 1901433, 2019.

[60] X. Cui, J. Yang, Z. Xu, Q. Liu, Y. Nuli, and J. Wang, "Highly stable lithium metal composite anode with a flexible 3D lithiophilic skeleton," *Nano Energy*, vol. 95, article 107013, 2022.

[61] Y. He, Y. Zhao, Y. Zhang et al., "Building flexibly porous conductive skeleton inlaid with surface oxygen- dominated MXene as an amphiphilic nanoreactor for stable Li-S pouch batteries," *Energy Storage Materials*, vol. 47, pp. 434–444, 2022.

[62] W. Wang, F. Hao, and P. P. Mukherjee, "Mechanistics of lithium-metal battery performance by separator architecture design," *ACS Applied Materials & Interfaces*, vol. 12, no. 1, pp. 556–566, 2020.

[63] P. Vadhva, J. Hu, M. J. Johnson et al., "Electrochemical impedance spectroscopy for all-solid-state batteries: theory, methods and future outlook," *ChemElectroChem*, vol. 8, no. 11, pp. 1930–1947, 2021.

[64] N. Cheng, X. Chen, and Z. Liu, "Iron porphyrin organic frameworks derived bionic-tree-nodule-like Fe7S8with ultralong potassium ion storage," *Energy & Fuels*, vol. 36, no. 1, pp. 694–702, 2022.

[65] J. He, A. Bhargav, and A. Manthiram, "Covalent organic framework as an efficient protection layer for a stable lithium-metal anode," *Angewandte Chemie International Edition*, vol. 134, no. 18, article e202116586, 2022.